Nano Energy 62 (2019) 844–852

Contents lists available at ScienceDirect

Nano Energy

journal homepage: www.elsevier.com/locate/nanoen

Review

Cooperative transport enabling fast Li-ion diffusion in Thio-LISICON $Li_{10}SiP_2S_{12}$ solid electrolyte

Bingkai Zhang[a,b], Luyi Yang[a], Lin-Wang Wang[b,**], Feng Pan[a,*]

[a] School of Advanced Materials, Peking University Shenzhen Graduate School, Shenzhen 518055, China
[b] Materials Sciences Division, Lawrence Berkeley National Laboratory, Berkeley, CA 94720, United States

ARTICLE INFO

Keywords:
Solid-state electrolyte
$Li_{10}SiP_2S_{12}$
Cooperative migration
Local configurations
Atomic simulations

ABSTRACT

LISICON-like materials are attracting attention as promising new Li-ion conductors with potential use in all-solid-state Li-ion batteries. Although the concept of cooperative diffusion mechanism has been discussed before, a detail understanding of the diffusion process is still lacking for this material. Here, an atomic-scale investigation of the $Li_{10}SiP_2S_{12}$ (LSPS)-based system using advanced simulation techniques provides valuable insights into its Li-ion conducting mechanisms. We find that Li-ion conduction in LSPS occurs through a concerted motion of interstitial and lattice Li-ions, evidenced both from molecular dynamics trajectory analysis and energy barrier calculations. The cause for the cooperative migration is the existence of a low-barrier step, by which one Li-ion's migration helps another adjacent Li-ion's migration through mutually beneficial S atoms relaxation and electrostatic interaction. Cooperative migration occurs in the channels formed by connected LiS_4 tetrahedrons through Li–Li interaction as well as dual-Li-sites. Cl-doping can enhance cooperative migration by a new low-barrier step due to more flexible PS_3Cl and large oscillation of Li, which smoothes Li potential energy surface and enhances cooperative migration.

1. Introduction

A range of rechargeable battery technologies are being investigated to satisfy the increasing demand of advanced energy storage systems [1]. In particular, the high energy density of all-solid-state lithium batteries (ASSLBs) and their potential high safety capability make them viable candidates for electric vehicles [2–6]. The ASSLBs require solid electrolytes with good Li-ion conductivity. In order to optimize the performance of solid electrolytes, fundamental understanding of ionic transport within a structure of a solid electrolyte is required [7–10].

Over the years, the sulfide LISICON-like materials have been proposed as promising candidates for inorganic solid electrolytes (ISEs) following the exciting discovery of cooperative migration in $Li_{10}MP_2S_{12}$ (M = Si, Ge, and Sn) family [11–15]. $Li_{10}MP_2S_{12}$ family shows the highest Li-ion conductivities above 10 mS/cm at room temperature [12]. Kato and Kanno et al. [16] reported $Li_{9.54}Si_{1.74}P_{1.44}S_{11.7}Cl_{0.3}$ (LSPSCl) solid electrolyte with the highest conductivity (25 mS/cm). These materials have a space group $P4_2/nmc$ and a body-centered cubic anion sub-lattice structure. In between the PS_4 and SiS_4 tetrahedra, four partially occupied Li sites are presented in the crystal structure. Therefore, multiple accessible sites are available for Li-ions, which causes occupation disorder.

A critical yet unanswered question is what is the atomic-scale mechanism controlling Li-ion transport in this system? Based on structural and geometrical considerations, possible Li-ion migration paths have been proposed [17,18]. Moreover, three explanations of Li-ions migrations have been proposed and they differ from each other on how movement of Li-ions is achieved [19–23]. The first explanation suggests that Li-ion conduction in ISEs occurs through an interstitial mechanism involving the concerted knock-on motion of interstitial and lattice Li-ions [19,20]. The second explanation is string-like migration pattern triggered by the electrostatic interaction among the mobile Li-ions when ISEs have high concentrations of mobile Li-ions [21]. The third explanation suggests Li-ions collectively hop into neighboring lattice Li-ion sites by kicking the Li-ions occupying these sites out [18,22,23]. In addition, Boris et al. [24] suggested that ionic transport is controlled by the frustration of the Li-sublattice because of incommensurability with the host structure at noninteger Li contents by theoretic calculations of garnet ISEs.

Given this situation, it is thus worthwhile to further investigate this situation by more careful analysis and tests. Intuitively, it seems more plausible that more than one Li-ions (Li–Li distance regularly exceeding

* Corresponding author.
** Corresponding author.
E-mail addresses: lwwang@lbl.gov (L.-W. Wang), panfeng@pkusz.edu.cn (F. Pan).

https://doi.org/10.1016/j.nanoen.2019.05.085
Received 12 October 2018; Received in revised form 5 May 2019; Accepted 30 May 2019
Available online 31 May 2019
2211-2855/ © 2019 Elsevier Ltd. All rights reserved.

3 Å) migration at the same time could induce large structural changes leading to reduce Li-ion migration barrier. Currently, although some studies for Li-ion cooperative transport in $Li_{10}MP_2S_{12}$ have been reported, the origin of cooperative migration remains unclear. Such investigations on the motivation for cooperative migration and how to implement it are rather limited. Such mechanistic details on relationship between the multi-Li-ions cooperative diffusion and local structure need to be explored to gain a deeper understanding of the macroscopic transport behavior that underpins potential strategies for optimizing the conductivity of ISEs, as well as designing next-generation materials.

In this work, we adopted atomistic (first principle calculations) and ab initio based molecular dynamics (AIMD) simulation techniques to probe the Li-ion transport mechanism by comparing with single Li-ion direct-hopping and two Li-ions cooperative migration, and their related Li-ion migration pathways, and the role of Cl dopants on the ionic conductivity of LSPSCl structure.

2. Computational details and structural models

All DFT calculations are carried out using the Vienna ab initio simulation package (VASP) [25] within the projector augmented wave (PAW) approach [26]. The generalized gradient approximation is adopted in the parameterization of Perdew, Burke, and Ernzerhof (PBE) to describe the exchange–correlation functional [27,28]. A supercell containing 4 formula units (f.u.) of $Li_{10}SiP_2S_{12}$ as a model was used. A k-mesh (3 × 3 × 2) was generated using the Monkhorst-Pack method to sample the Brillouin zone. The evaluation of the migration barrier of Li-ion is carried out by the climbing image nudged elastic band (cNEB) method as implemented in VASP [29]. The Li-ion dynamics are performed using the AIMD under the NVT ensemble (at T = 300, 400, 500, 600 and 700 K) and Nosé thermostat to give a simulation time of 30 ps. The ionic trajectories analyses of AIMD simulations use Python Materials Genomics (pymatgen) [30] and its add-on package pymatgen-diffusion [31]. NVT AIMD simulation is also used to calculate the Li-ion diffusion coefficient (D_{Li}) and predict the room temperature conductivity (σ_{Li}). The calculation details of D_{Li} and σ_{Li} are present in supporting information (SI).

The crystal structure of LSPS has tetragonal symmetry and is composed of isolated SiS_4 and PS_4 units with no sharing S, which form two channels along c and ab-plane (Fig. 1a). On the other hand, it is useful to image the LiS_4 tetrahedral sharing S from different SiS_4 and PS_4 tetrahedrals. The Li-ion diffusion pathways are highlighted by the LiS_4 tetrahedral configurations and sketches in Fig. 1b (but not all the LiS_4 are occupied with Li at its center for a given configuration snapshot).

To construct the Cl-doped LSPS system, an S atom in LSPS is substituted with a Cl atom. In modeling the Cl-doped LSPS system, the formation of Li vacancy in LSPS is considered because the substitution of Cl^- for S^{2-} can be charge-balanced by the formation of Li vacancy at the adjacent site. The detail for formation energy is described in SI. Fig. S1 presents the calculated Cl-dopant formation energies as functions of the Fermi level [32]. For Fermi energy above valence band maximum (VBM), the formation energies of neutral state of Cl_S^0 is under the intersection of the Cl_S^{+1} and Cl_S^{-1}, suggesting neutral state of Cl_S^0 is the most favorable one in LSPSCl. We also check the Cl-dopant at an interstitial site. Fig. S2 shows that formation of interstitial Cl-dopant in LSPS is only favorable under extreme high chemical potential of Cl. Under the chemical potential of Cl defined by LiCl, the formation energy of interstitial Cl is about 3.8 eV. Therefore, LSPSCl structure with neutral state of Cl_S^0 is the most thermodynamically favorable one, which is consistent with experimental observation [16].

For the Li channel along the c-axis, there are two types of tetrahedral distinguished by their shapes, denoted as 1 and 2 with occupied Li_1 and Li_2, respectively. They can also be divided into two types: 1, 1′ types and 2, 2′ types due to orientation difference. Since 1 and 1′ sites are close together, they will also be called dual-Li-sites. Along the possible path on the ab-plane, there is another Li-site which we call site 3 with occupied Li_3, with 6-S atom surrounding this site. The channels are consisted of edge-sharing LiS_4 units along c-axis and edge-sharing or point-sharing polyhedron LiS_x units along ab-plane. The $Li_{1/1'}$ and $Li_{2/2'}$ tetrahedrons make up the c-axis channel, and $Li_{1/1'}$ and Li_3 polyhedrons make up the ab-plane channel. Due to the symmetry of the system, Li_1 and $Li_{1'}$ are two equivalent positions, similarly for Li_2 and $Li_{2'}$. The distance for adjacent $Li_{1/1'}$ sites (assigned dual-Li-sites) is about 1.4 Å, which is much shorter than that of Li–Li regular distance (> 3 Å), so double occupancy of the two sites is highly unfavourable (by over 1.80 eV according to our calculation). Fig. 1c shows optimized LiS_4 tetrahedrons along the c-axis and ab-plane, both with three Li-ions in the unit cell.

3. Results and discussion

3.1. Stability of LSPS and LSPSCl

Phase stability of LSPS and LSPSCl is analyzed after computing the decomposition energy ($\Delta E_{decomposition}$) of LSPS or LSPSCl with respect to the possible decomposition compounds. $\Delta E_{decomposition}$ is defined as

$$\Delta E_{decomposition}(\text{LSPS/LSPSCl}) = E(\text{LSPS/LSPSCl}) - E(\text{decomposition compounds}). \quad (1)$$

The negative value of $\Delta E_{decomposition}$ means the decomposition is unfavourable. Here, we consider three combinations for LSPS: 1) $Li_{10}SiP_2S_{12} = 2Li_3PS_4 + Li_4SiS_4$, 2) $Li_{10}SiP_2S_{12} = P_2S_5 + 5Li_2S + SiS_2$, and 3) $Li_{10}SiP_2S_{12} = 2Li_3PS_4 + 2Li_2S + SiS_2$; and one combination for LSPSCl: $Li_{19}Si_2P_4S_{23}Cl = 2P_2S_5 + 9Li_2S + 2SiS_2 + LiCl$. The coefficients for all the decomposition compounds are positive. The calculated formation energies are listed in Table 1. The large negative values in Table 1 mean the LSPS (−69.08 meV/atom) and LSPSCl (−50.38 meV/atom) are thermodynamically stable with respect to the equilibrium phase decomposition to binary P_2S_5, Li_2S, SiS_2, and LiCl. The favorable decomposition case for LSPS is decomposition into the ternary compound (Li_3PS_4) and binary compounds (Li_2S and SiS_2) with a decomposition energy of 1.21 meV/atom, as shown in Fig. 2a constructed by open quantum materials database [33] in Materials Project [34]. Similar to LSPS, LSPSCl could easily decompose into Li_3PS_4 and binary compounds (Li_2S, LiCl and SiS_2), with a decomposition energy of 19.22 meV/atom. Although this is positive, but it is extremely small, probably within the limitation of the DFT accuracy. On the other hand, recent experimental endeavor demonstrates the synthesis and ionic conductivity of LSPSCl [16]. Thus, thermodynamic meta-stability leading to the solid-solid phase decomposition is less problematic in practice due to the associated kinetic barrier.

To verify their practical application, we evaluate the interfacial and compatibility against to Li-metal anode and several cathodes. First, we evaluate the electrochemical stability of LSPS/LSPSCl against Li reduction (from 0 to 5 V) by the Li grand potential phase diagrams, as shown in Fig. 2b and c. The stable phases at different voltage are also listed in Fig. 2b and c. The stability window is determined after consideration of the energy of the lithium extraction or insertion without any mixing reaction between LSPS/LSPSCl and Li. We note the narrow stability window of LSPS and LSPSCl is similar from 1.7 to 2.2 V, indicating Cl-dopant does not significantly alter the stability of LSPS against Li reduction.

To understand the interfacial electrochemistry between LSPS/LSPSCl with cathodes, we consider all possible reactions of the form x (LSPS/LSPSCl) + (1-x)(Cathode) → $c_{equilibrium}$, where $c_{equilibrium}$ is the low energy phase equilibrium determined from the phase diagram, and x is the mixing parameter varying from 0 to 1. Thermodynamically feasible chemical reaction between the LSPS/LSPSCl and cathodes ($LiXO_2$, X = Ni, Co, and Mn, $LiFePO_4$, $LiMn_2O_4$) are detailed in Figs. S3 and S4 of SI. We find that compared to the LSPS, LSPSCl shows lower reaction energies with oxide cathodes. LSPS undergoes the

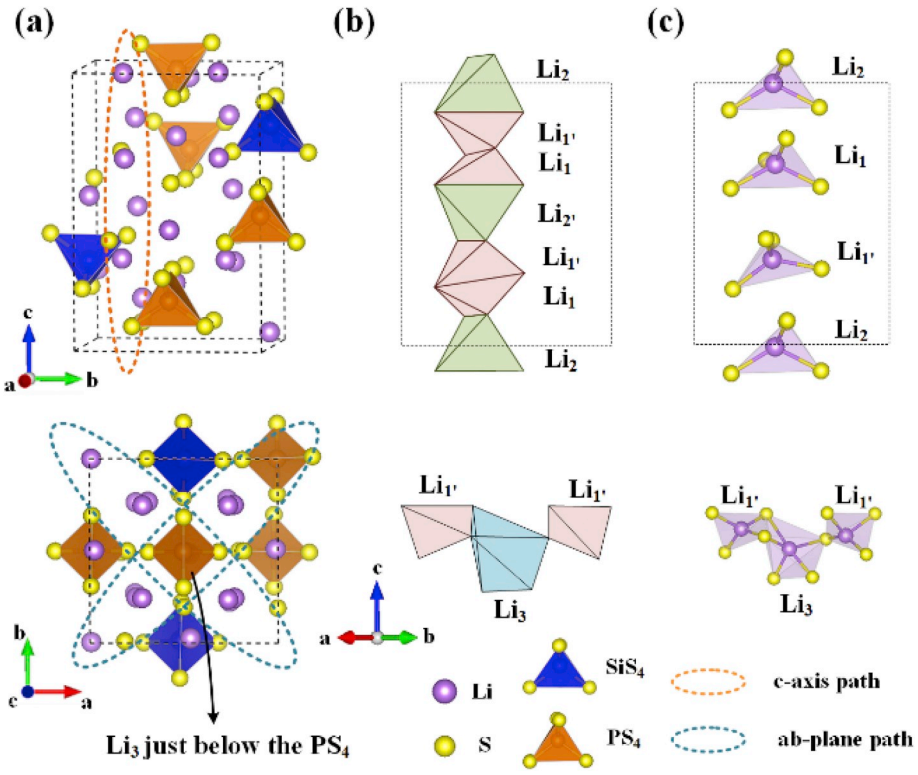

Fig. 1. (a) Schematic of LSPS and the diffusion paths. (b) Illustration of Li-ions occupying the spaces of LiS_4 tetrahedrons and the connection between tetrahedrons. Dual-Li-sites are labelled as Li_1 and $Li_{1'}$ due to their short distance. (c) Typical LiS_4 configurations along c-axis and ab-plane.

transformation to phosphates (with PO_4 units) and transition metal sulfides (M_xS_y, M = Ni, Co, Mn and Fe). The predominance of Li_3PO_4 as the interfacial composition can facilitate the Li-passivation in LSPS and LSPSCl. The results in Figs. S3 and S4 also suggest the favorable combination is $LiFePO_4$ combined with LSPS or LSPSCl, which exhibits minimal reaction energy.

In summary, the LSPS and LSPSCl is thermodynamically stable against the decomposition to binary sulfide and LiCl. The cathodic and anodic limit for LSPS/LSPSCl is about 1.7 and 2.2 V, respectively. The LSPS/LSPSCl can undergo chemical reaction with high voltage of oxide cathodes ($LiXO_2$) and the possible combination is $LiFePO_4$–LSPS/LSPSCl.

3.2. Li-ion diffusion in LSPS by AIMD calculations

In order to study the detailed migration pathway in LSPS, we first carried out AIMD NVT calculations under different temperatures. As temperature increases, Li-ions become delocalized from their initial sites, leading to Li-ions diffusion. Such techniques are well suited to probe Li-ions transport mechanism directly since ionic conductivity is temperature dependence.

The overall Li-ions trajectory density during the AIMD simulation enables the diffusion pathways to be visualized. Under the temperature of 400 K, the shape and size of the density in Fig. 3a shows Li-ions diffusion paths within this system which is anisotropic, restricted exclusively to the channels along c-axis with no obvious evidence of Li-ion diffusion in the ab-plane. In comparison, the trajectory density of Li-ions under the temperature of 600 K in Fig. 3b shows ab-plane diffusion through the Li_3 sites. These results suggest that Li-ion migration occurs preferentially along c-axis, especially at lower temperature.

For detailed analysis, in Fig. 4 we have focused, as selected examples, on trajectory density of different Li-ions along c-axis, distinguished by their color. First, at low temperature (300 K), the distribution of trajectories in Fig. 4a suggests the motion of Li-ions are constrained with only a local oscillation of Li-ions. However, the trajectory size of dual-Li-sites (Li_1 and $Li_{1'}$) is greater than that of $Li_{2'}$, suggesting a high mobility of $Li_{1/1'}$. To examine this point further, we compared the site displacement function (SDF) of Li_1 and $Li_{2'}$ as a function of simulation time. The SDF equation is defined $d(t) = |r(t) - r(0)|$, i. e, the distance between the position of the Li-ion at time t ($r(t)$) and the initial position of the Li-ion atom at time 0)). The SDF results (Fig. 4b) of Li_1 have higher divergence than that of $Li_{2'}$, which is consistent with the trajectory density plots.

It is useful to understand why dual-Li-sites have higher mobility. For this, we analyzed the structures of c-axis channel connected by edge-sharing LiS_4 tetrahedrons. These edges are relevant to bottleneck of Li-ions diffusion. Fig. S5 in SI shows the sharing-edges length distribution probability over 30 ps NVT AIMD simulation (T = 300 K). The results

Table 1
Phase stability ($E_{decomposition}$) of LSPS and LSPSCl with respect to equilibrium.

Compound	Decomposition equation	Decomposition energy (meV/atom)
LSPS	$Li_{10}SiP_2S_{12} = 2Li_3PS_4 + Li_4SiS_4$	−57.36
	$Li_{10}SiP_2S_{12} = P_2S_5 + 5Li_2S + SiS_2$	−69.08
	$Li_{10}SiP_2S_{12} = 2Li_3PS_4 + 2Li_2S + SiS_2$	1.21
LSPSCl	$Li_{19}Si_2P_4S_{23}Cl = 2P_2S_5 + 9Li_2S + 2SiS_2 + LiCl$	−50.38
	$Li_{19}Si_2P_4S_{23}Cl = 4Li_3PS_4 + 3Li_2S + 2SiS_2 + LiCl$	19.92

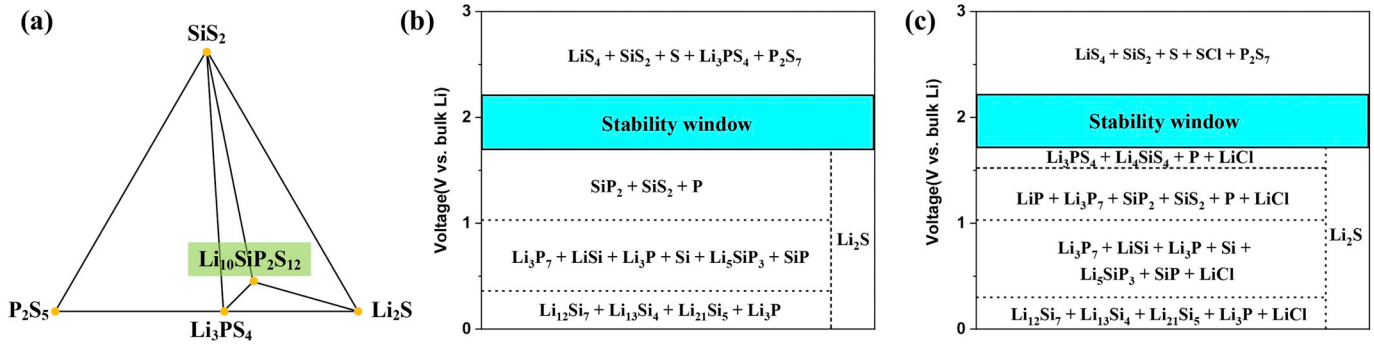

Fig. 2. (a) The Li_2S–P_2S_5–SiS_2 phase space with $Li_{10}SiP_2S_{12}$ appeared. (b) and (c) Electrochemical stability windows of LSPS and LSPSCl. The voltage profile and phase equilibria of LSPS and LSPSCl upon lithiation and de-lithiation that determine the anodic and cathodic reactions are shown.

suggest that the sharing-edge between Li_1 and $Li_{1'}$ sites is larger than others, which explains the easier Li-ion transfer from one site to another.

At 400 K, the shape of trajectory density distribution in Fig. 4c suggests all Li-ions undergo a jump motion from initial to neighboring sites in one direction. In upper inset of Fig. 4d, the intensity of Li_1-ion displacement around 10 ps increases suddenly with the simulation time and stays around this intensity for 5 ps at least. This increase shows that Li_1 is displaced for distance larger than 1.0 Å. This appearance of this transition is the signal for Li-ion jumping into its neighboring site and staying on that site for 5 ps at least. A similar phenomenon is observed for Li_2 and $Li_{1'}$ (below insets of Fig. 4d): a sudden increase of Li-ion displacement around 10 ps, staying on that site for some time (around 5 ps) then jumping to achieve a displaced distance larger than 2.0 Å around 15 ps, suggesting that Li-ions jump into new sites other than the ones at t = 0. Furthermore, the three Li-ions' jumping occurs at almost the same time (e.g., at 10 ps in Fig. 4d), suggesting correlated motion.

Considering the high mobility of dual-Li-sites, Li-ions diffusion is likely to be initiated by the motion of Li_1, followed by the $Li_2 \rightarrow Li_1$ and $Li_{1'} \rightarrow Li_{2'}$ shown in Fig. 4c. We also give the trajectory density distribution and SDF of Li-ions along ab-plane in Fig. 4e and f. An important feature is that the diffuse distribution and overlapping of $Li_{1'}$ and Li_3 positions indicates that Li-ions are moving along ab-plane. The SDF in Fig. 4f suggests that $Li_{1'}$ ion resides at an interstitial site (Li_i) for ~2 ps and then displaces a Li_3 ion into a neighboring a Li_1 site.

3.3. Li-ion migration by cNEB calculations

After we analyzed the AIMD path, we now calculate the energy profile by cNEB method, thus provide an energetic picture for different diffusion path. The merit of cNEB calculation is that it models local lattice relaxation around the migrating Li-ions and, therefore, other atoms such as S atoms are not treated simply as hard-sphere lattice of fixed ions. In the cNEB calculations the configurations for single Li-ion migration and multi-Li-ions cooperative migration can be investigated separately, thus their perspective barrier heights can be compare.

Fig. 5 shows the energy profile of single Li-ion migration. We find that the migration between $Li_{1/1'}$ sites (step 1) is very easy with low energy barrier (~0.09 eV) but the migrations of Li_1 to $Li_{2'}$ sites (step 2) and Li_2 to Li $_1$ sites (step 3) are difficult with high energy barrier (~0.31 eV). Therefore, step 1, $Li_1 \rightarrow Li_{1'}$ migration, is a low-barrier step. This finding is consistent with the high Li mobility between dual-Li-sites (Li_1 to $Li_{1'}$) observed using AIMD techniques.

Fig. 6a shows the energy profile of multi-Li-ions cooperative migration with the important states along the pathway, namely, IS1 (initial state), MS1 (meta-stable intermediate), FS1 (final state), IS2 (same configuration as FS1), MS2, and FS2 (same configuration as IS1). The diffusion steps become IS1 → MS1 → FS1 (IS2) → MS2 → FS2 (IS1) as shown in Fig. 6b. The detailed intermediate (IM) configurations are shown in Figs. S6 and S7 in SI. The whole migration can be divided into two steps. 1) Li_1 moves to $Li_{1'}$ site while $Li_{2'}$ moves to edge position between $Li_{2'}$ and $Li_{1'}$ sites (step 4). From MS1, Li_1 migrates into the $Li_{1'}$ site and $Li_{2'}$ migrates into an edge site. 2) $Li_{2'}$ and $Li_{1'}$ approach to lattice sites at the same time (step 5). In step 5, one Li moves in the dual-Li-sites and the other Li jumps out the dual-Li-sites. We recall that section 2.1 shows that double occupancy of the dual-Li-sites is highly unfavourable. Therefore, the dual-Li-sites configuration serves to highlight the cooperative migration by electrostatic repulsion. This energy profile indicates that meta-stable intermediate (MS1, which is at edge positions between $Li_{2'}$ and $Li_{1'}$ sites) is actually a local energy minimum. The calculated energy barrier of complete migration is about 0.22 eV.

Next, we studied Li-ion migration along ab-plane in LSPS as shown in Fig. 7. In the configuration structure, the large space between $Li_{1'}$ and Li_3 creates a Li-ion interstitial site, namely Li_i. For single Li-ion direct-hopping (Fig. 7a), the calculated barriers for step 8 to 10 are ~0.35 eV ($Li_3 \rightarrow Li_1$), ~0.12 eV ($Li_{1'} \rightarrow Li_i$), and ~0.21 eV ($Li_1 \rightarrow Li_3$), respectively. Therefore, step 9, $Li_{1'} \rightarrow Li_i$ migration, is a low-barrier step,

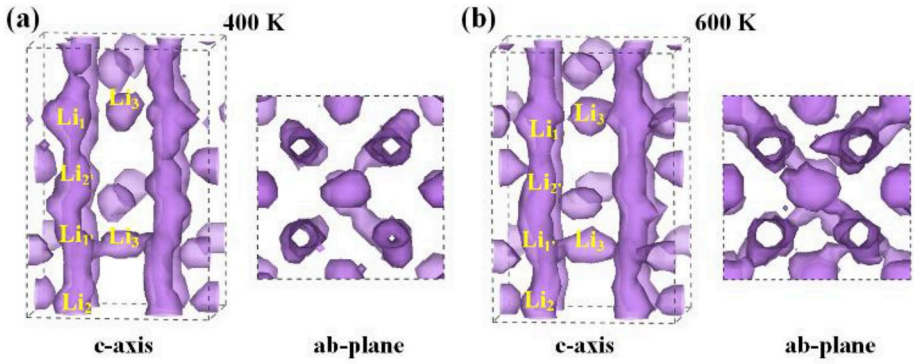

Fig. 3. (a) and (b), the trajectory density (1×10^{-3} Å^{-3} isosurface level) of Li-ions in LSPS taken from 30 ps NVT AIMD simulations at 400 K and 600 K.

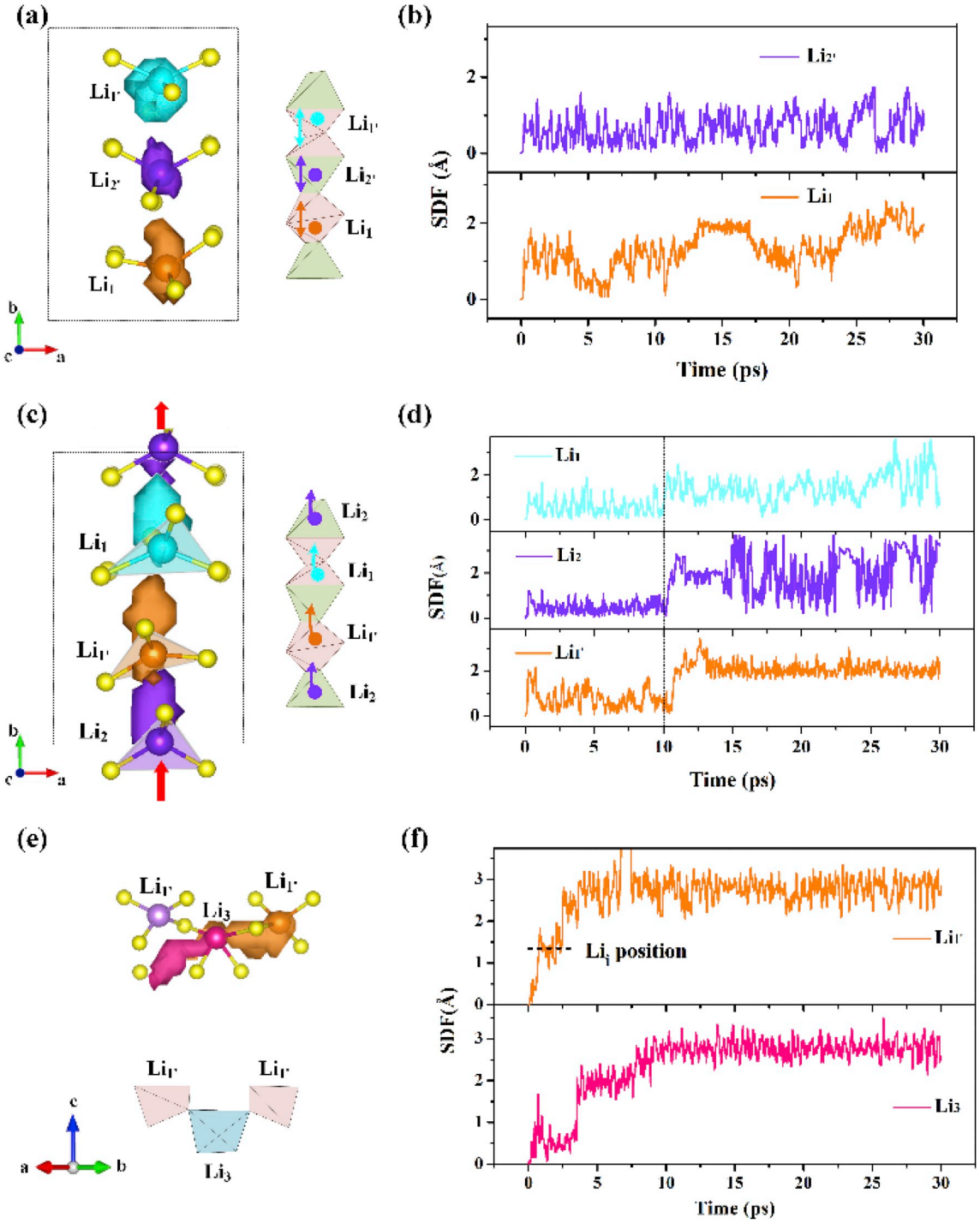

Fig. 4. The trajectory density of Li-ions (3×10^{-3} Å^{-3} isosurface level), and SDF plots for Li-ion trajectories in the AIMD simulation. (a) and (b) are plotted at 300 K along c-axis. (c) and (d) are plotted at 400 K along c-axis. (e) and (f) are plotted at 600 K along ab-plane. The right insets of (a) and (c) are the schematic of the Li-ions diffusion. The black dashed line in (d) suggests the time nodes for Li-ions hopping. The black dashed line in (f) suggests an interstitial position. The yellow balls are S atoms. (For interpretation of the references to color in this figure legend, the reader is referred to the Web version of this article.)

which is also suggested by the trajectory density and SDF of $Li_{1'}$ as shown in Fig. 3f. For cooperative migration (Fig. 7b), the energy profile along with sketches of key configurations suggests the whole migration also includes two steps: 1) $Li_{1'} \rightarrow Li_i$ migration (step 11); 2) Li_i and Li_3 migrate to the neighboring lattice sites at the same time (step 12). Here, the metastable intermediate, MS3, is again a local energy minimum. The calculated energy barrier is ~0.29 eV, suggesting cooperative migration is more favorable than single Li-ion direct-hopping. However, the energy barrier is slightly higher than that along c-axis. Using microkinetics and assuming the same pre-exponential factor in the Arrhenius relationship (300 K), it can be estimated that the diffusion coefficient of Li-ions along c-axis is about fifteen times of that along ab-plane.

The difference between the single ion paths shown in Fig. 5 and cooperative path of Fig. 6 is that, for single ion, only one ion moved and the local minima are the configurations where all Li atoms are in the LiS_4 tetrahedral centers, while for cooperative migration, two Li atoms move, and the higher energy metastable states are for Li atoms at the

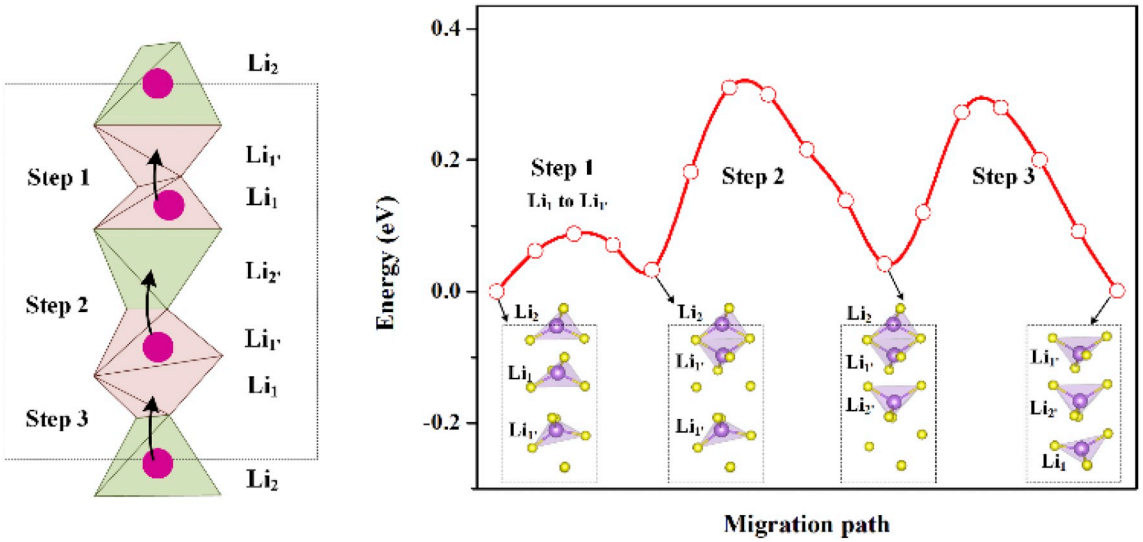

Fig. 5. The sketch and energy profile of single Li-ion direct-hopping migration via three migration steps along c-axis.

edges between two tetrahedral, which can change the transition state (TS) structure and smooth the transition path of Li-ion migration. Fig. S8 in SI provides an illustration of TS-1 (single ion path) and TS-2 (two ions cooperative path) to help understand this point. In TS-2, Li_1 moves to the edge site of dual-Li-sites, the distance between S_7 and S_8, i.e. the length of sharing-edge in $Li_{(1')}S_4$–$Li_{(2')}S_4$, is 4.52 Å, whilst it is 4.23 Å in TS-1. As a result, the distance between the $Li_{2'}$ and the S_7 and S_8 at is 2.57 and 2.58 Å at TS-2, which is ~0.12 Å longer than that inTS-1. Therefore, the $Li_{2'}$ can get away from $Li_{(2')}S_4$ tetrahedron with the aid of the Li_1 migration, in which the TS has better contact with both the $Li_{2'}$ (bonding with S_9 and S_{10}) and Li_1 (bonding with S_7 and S_8) and reduces the barrier of the $Li_{(2')}$-S_7 and $Li_{(2')}$-S_8 bond breaking. Therefore, the migration of dual-Li-site can better stabilize the TS by means of mutually beneficial S atom relaxation, which reduces the barrier of Li-ions migration.

From energy point of view, the calculated results support the previous opinion that cooperative migration is due to the energy difference of adjacent Li-sites [23]. In short, during the cooperative migration of two Li-ions, the Li-ions located at the high-energy sites migrate downhill, which cancels out the energy barriers for other uphill-climbing Li-ions, which lowers the overall barrier. In our cases of cooperative

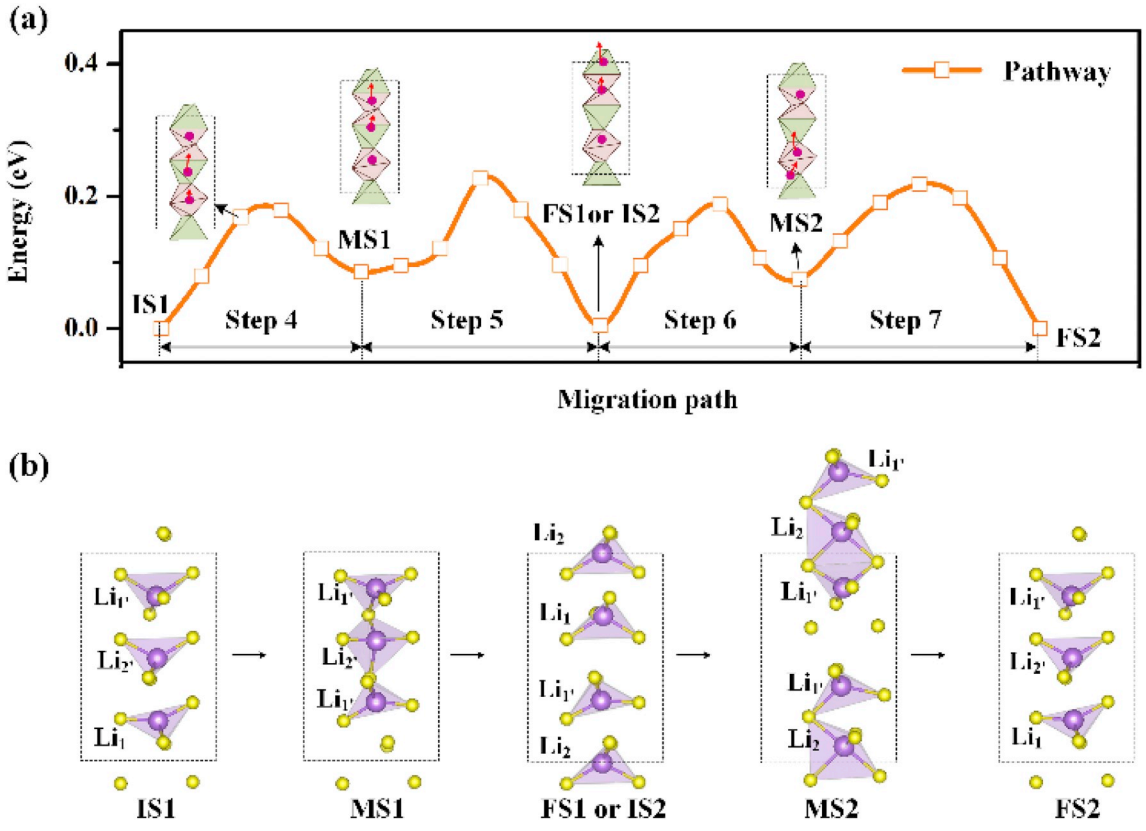

Fig. 6. (a) The energy profiles and sketches of Li-ion cooperative migration along c-axis via two stages. (b) The geometric configurations of IS, MS and FS along migration pathway.

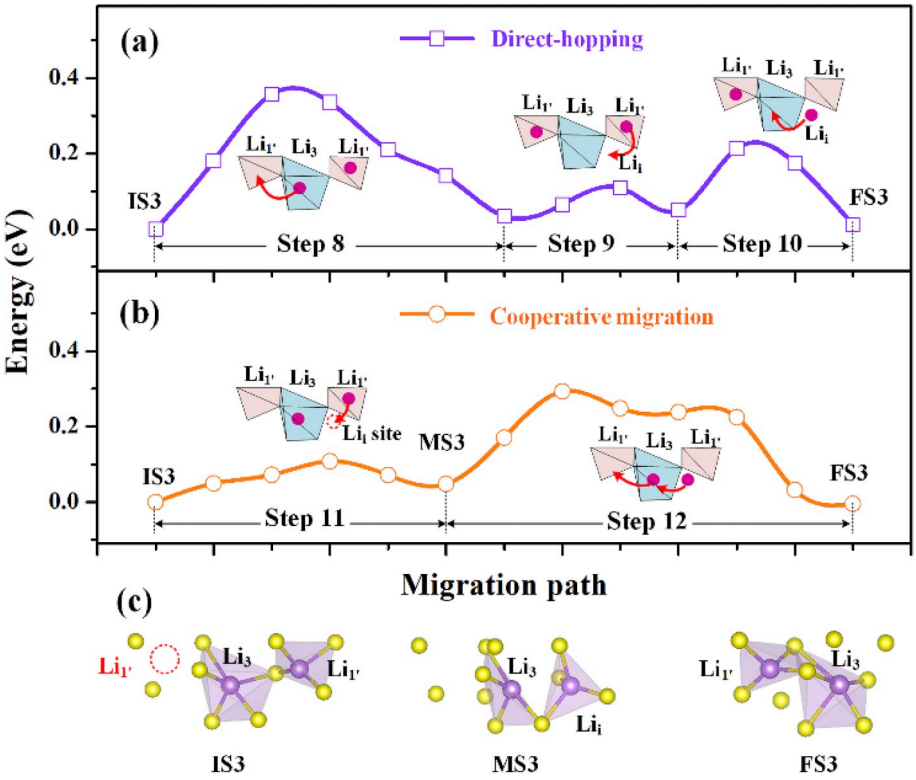

Fig. 7. (a) and (b) The energy profiles and sketches of single Li-ion direct-hopping migration and Li-ions cooperative migration along ab-plane. (c) The geometries of IM3, MS3 and FS3 for Li-ions cooperative migration.

migration, a common feature is found that one Li-ion is at a metastable edge site while the other Li-ion is at tetrahedral center site. In contrast, Fig. 5 shows that for single Li-ion diffusion along c-axis, the energy valley always resides at the central tetrahedral site with low energy, and energy peak is at the sharing-edge between tetrahedrons with high energy.

In summary, the motion of LBS helps neighboring Li-ion to overcome a high-barrier step via mutually beneficial S atom relaxation, thereby forming a metastable structure at which allows electrostatic repulsion to give extra-force to push lattice Li-ions and smooths the energy profile of Li-ions.

3.4. Effects of Cl-dopant on Li-ion migration

Cl-doping can greatly enhance the conductivity of LSPS [16], it is thus necessary to understand the Cl-mediated mechanism and the effects of Cl-dopant on cooperative migration. Two Cl-doping configurations are optimized based on the experimental conclusion that Cl-dopants replace S-atoms in LSPS, as shown in right insets of Fig. 8a and b. In case I, Cl-dopant resides at sharing-edge of dual-Li-sites, which enlarges the volume of dual-Li-sites because of long bonds: Li–Cl (2.74 Å) and Cl–S (4.71 Å). In case II, Cl-dopant resides at the sharing-edge in $Li_{(2)}S_4$–$Li_{(1)}S_4$, which again enlarges the volume of the two tetrahedrons because of long bonds, Li–Cl (2.72 Å) and Cl–S (4.59 Å).

Next, we estimate the diffusivity of LSPS and LSPSCl as shown in Fig. S9. The room temperature Li diffusion coefficient (D_{Li}) within LSPSCl (1.6×10^{-7} cm^2/s) is larger than that for LSPS (8.8×10^{-8} cm^2/s). Consequently, the room temperature (298 K) Li-ion conductivity for LSPSCl is about 20.0 mS/cm, which is also larger than that of LSPS (11.0 mS/cm). Therefore, we propose LSPSCl as an affordable Li-superionic conductor.

To understand this enhancement of Cl-dopant on ionic conductivity, we obtain their trajectory densities of Li-ions from NVT AIMD (T = 400 K) shown in left insets of Fig. 8a and b. Comparison of the shape of trajectory density with that of LSPS in Fig. 3, Cl-dopants leads to a new diffusion channel in case I (Fig. 8a). Radial distribution functions (RDFs) for Li–S and Li–Cl calculated during simulation time are shown in Fig. 8c. The sharp peaks centered at about 2.50 Å and 2.70 Å for the Li–S and Li–Cl separations, suggest that the average bond length of Li–Cl is larger than that of Li–S. Furthermore, the angle trajectories for ∠Cl–P–S and ∠S–P–S during simulation time are shown in Fig. 8d. The results suggest that the average angle for ∠S–P–S is always close to the ideal value whereas that for ∠Cl–P–S has considerable fluctuations, indicating the rotation motion of the $PClS_3$ tetrahedral units and flexibility of the structure. The flexibility of Cl related structure make it easy for Li to pass through, since during the transition point it is necessary to deform the tetrahedron. The above result indicate that Cl-dopants liberate adjacent Li-ion and promote Li-ion migration.

To further examine the influence of Cl-dopant on structures during Li-ion migration,We also calculated the single Li-ion hopping within $Li_{(2)}S_3Cl$–$Li_{(1)}S_3Cl$ of case II. The calculated barrier for above step is about 0.13 eV, suggesting a low-barrier step in case II but it is 0.31 eV in LSPS (step 3 in Fig. 5). To prove this, we compared the SDF of Li_2-ions (within $Li_{(2)}S_4$ and $Li_{(2)}S_3Cl$) (Fig. 9). The SDF results show that the displacement of Li from $Li_{(2)}S_3Cl$ tetrahedron is much larger than that from $Li_{(2)}S_4$. The above result indicate that Cl-dopants liberate adjacent Li-ion and promote Li-ion migration. In case II configuration, the cooperative migration barriers along c-axis and ab-plane are lowered to 0.19 and 0.22 eV, respectively, as shown in Fig. S10. This finding implies that Cl-dopant could further enhance migration by the new low-barrier step due to $Li_{(2)}S_3Cl$.

4. Conclusion

The Li-ion transport mechanism of LSPS and LSPSCl in $Li_{10}MP_2S_{12}$ family, including atomic structure, Li-ion transport mechanism and ion diffusion barriers, are investigated using AIMD and ground state barrier

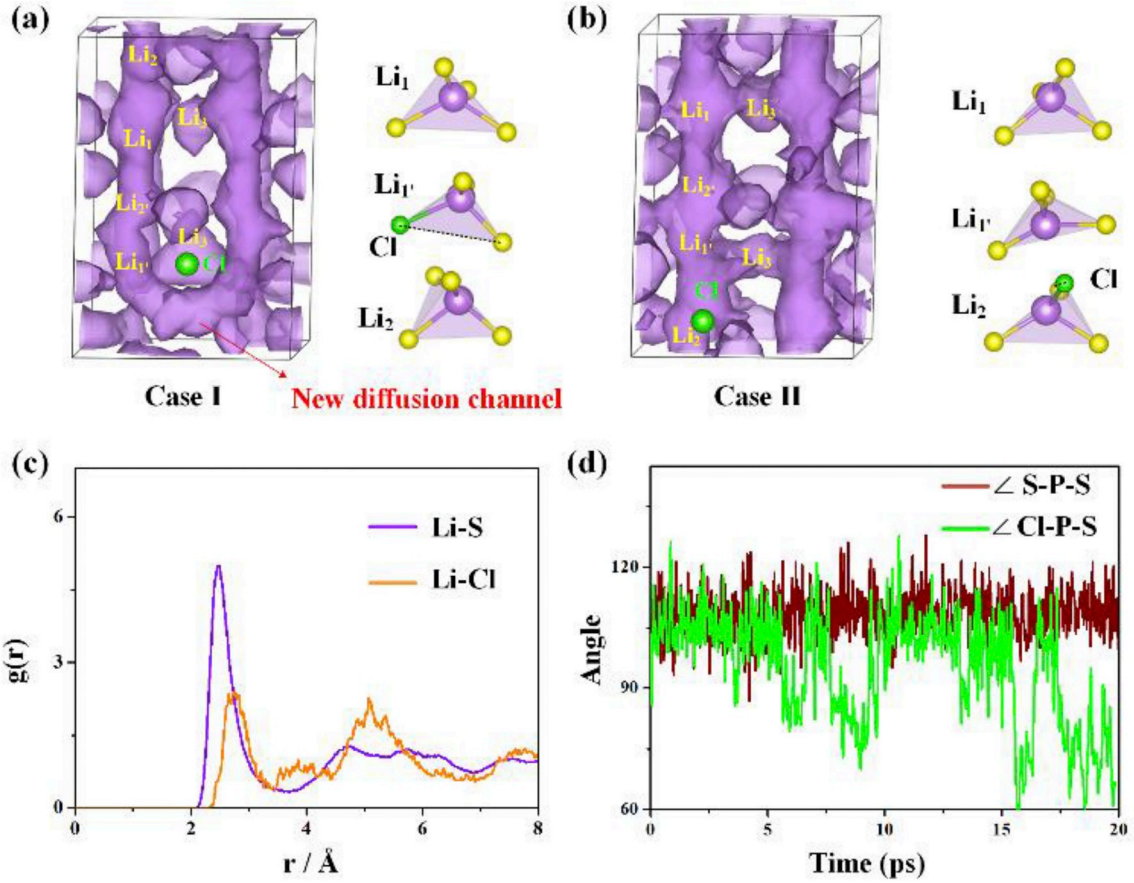

Fig. 8. (a) and (b) The trajectory density (1×10^{-3} Å^{-3} isosurface level) of Li-ions in LSPS taken from 30 ps NVT AIMD simulations at 400 K. (c) RDFs for Li–S and Li–Cl interactions. (d) The angle change trajectory over the 30 ps NVT AIMD simulations at 400 K.

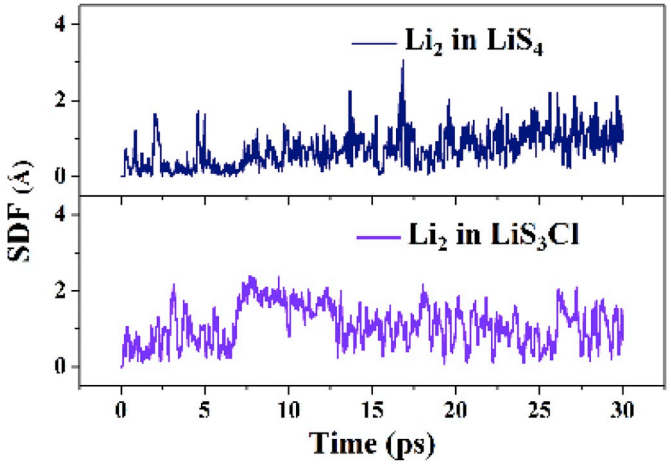

Fig. 9. SDF plots for Li_2 trajectories in the AIMD simulation at 300 K in LSPSCl.

height calculations. Multi-Li-ions cooperative migration creates fast Li-ion conduction for LISICON-like $Li_{10}MP_2S_{12}$ ISEs.

Three discoveries are summarized here. First, Li-ion migration follows cooperative migration mechanism involving the concerted motion of shared-edge Li site and tetrahedral center site. While the shared-edge site is a higher energy site for Li, the tetrahedral site is a low energy site for Li. It is due to the cooperative transition between the Li-ions at these two sites which makes the total energy of the transition path smooth, and results in a lower barrier. Second, cooperative migration comes from a low-barrier migration step caused by a favorable LiS_4 configuration along the channels of c-axis and ab-plane, i.e. dual-Li-sites. This leads to a metastable intermediate with a more favorable local bonding geometry of the Li and S atoms, which makes the TS geometry stable. An important determining factor of this transport mechanism is the flexibility of PS_4 units. As the transition point requires the deformation of the LiS_4 tetrahedron, a flexible PS_4 unit (e.g. being able to rotate) will lower the barrier height. Third, Cl-doping enhances cooperative migration by making the corresponding $SiClS_3$ units more flexible, which leads to new low-barrier step or a new diffusion channel.

Acknowledgements

This work was supported by Soft Science Research Project of Guangdong Province (No. 2017B030301013), Shenzhen Science and Technology Research Grant (ZDSYS201707281026184). Wang was supported by the Assistant Secretary for Energy Efficiency and Renewal Energy of the U.S. Department of Energy under the Battery Materials Research (BMR) program.

Appendix A. Supplementary data

Supplementary data to this article can be found online at https://doi.org/10.1016/j.nanoen.2019.05.085.

References

[1] M.S. Islam, C.A.J. Fisher, Chem. Soc. Rev. 43 (2014) 185.
[2] J.A. Dawson, P. Canepa, T. Famprikis, C. Masquelier, M.S. Islam, J. Am. Chem. Soc. 140 (2018) 362.
[3] H. Duan, Y.-X. Yin, Y. Shi, P.-F. Wang, X.-D. Zhang, C.-P. Yang, J.-L. Shi, R. Wen, Y.-G. Guo, L.-J. Wan, J. Am. Chem. Soc. 140 (2018) 82.
[4] R. Chen, W. Qu, X. Guo, L. Li, F. Wu, Mater. Horiz. (2016) 487.
[5] Y. Xiayin, H. Bingxin, Y. Jingyun, P. Gang, H. Zhen, G. Chao, L. Deng, X. Xiaoxiong,

Chin. Phys. B 25 (2016) 018802.
[6] J.C. Bachman, S. Muy, A. Grimaud, H.-H. Chang, N. Pour, S.F. Lux, O. Paschos, F. Maglia, S. Lupart, P. Lamp, L. Giordano, Y. Shao-Horn, Chem. Rev. 116 (2016) 140.
[7] F. Han, Y. Zhu, X. He, Y. Mo, C. Wang, Adv. Energy Mater. 6 (2016) 1501590.
[8] B. Zhang, R. Tan, L. Yang, J. Zheng, K. Zhang, S. Mo, Z. Lin, F. Pan, Energy Storage Mater 10 (2018) 139.
[9] Y. Deng, C. Eames, B. Fleutot, R. David, J.-N. Chotard, E. Suard, C. Masquelier, M.S. Islam, ACS Appl. Mater. Interfaces 9 (2017) 7050.
[10] Y. Deng, C. Eames, J.-N. Chotard, F. Lalère, V. Seznec, S. Emge, O. Pecher, C.P. Grey, C. Masquelier, M.S. Islam, J. Am. Chem. Soc. 137 (2015) 9136.
[11] J. Yin, X. Yao, G. Peng, J. Yang, Z. Huang, D. Liu, Y. Tao, X. Xu, Solid State Ionics 274 (2015) 8.
[12] N. Kamaya, K. Homma, Y. Yamakawa, M. Hirayama, R. Kanno, M. Yonemura, T. Kamiyama, Y. Kato, S. Hama, K. Kawamoto, A. Mitsui, Nat. Mater. 10 (2011) 682.
[13] Y. Mo, S.P. Ong, G. Ceder, Chem. Mater. 24 (2012) 15.
[14] D.A. Weber, A. Senyshyn, K.S. Weldert, S. Wenzel, W. Zhang, R. Kaiser, S. Berendts, J. Janek, W.G. Zeier, Chem. Mater. 28 (2016) 5905.
[15] S.P. Ong, Y. Mo, W.D. Richards, L. Miara, H.S. Lee, G. Ceder, Energy Environ. Sci. 6 (2012) 148.
[16] Y. Kato, S. Hori, T. Saito, K. Suzuki, M. Hirayama, A. Mitsui, M. Yonemura, H. Iba, R. Kanno, Nat. Energy 1 (2016) 16030.
[17] O. Kwon, M. Hirayama, K. Suzuki, Y. Kato, T. Saito, M. Yonemura, T. Kamiyama, R. Kanno, J. Mater. Chem. 3 (2015) 438.
[18] S. Nishino, T. Fujiwara, H. Yamasaki, Phys. Rev. B 90 (2014).
[19] S. Shi, P. Lu, Z. Liu, Y. Qi, L.G. Hector, H. Li, S.J. Harris, J. Am. Chem. Soc. 134 (2012) 15476.
[20] Y. Yang, Q. Wu, Y. Cui, Y. Chen, S. Shi, R.-Z. Wang, H. Yan, ACS Appl. Mater. Interfaces 8 (2016) 25229.
[21] M. Xu, J. Ding, E. Ma, Appl. Phys. Lett. 101 (2012) 031901.
[22] F. Du, X. Ren, J. Yang, J. Liu, W. Zhang, J. Phys. Chem. C 118 (2014) 10590.
[23] X. He, Y. Zhu, Y. Mo, Nat. Commun. 8 (2017) 15893.
[24] B. Kozinsky, S.A. Akhade, P. Hirel, A. Hashibon, C. Elsässer, P. Mehta, A. Logeat, U. Eisele, Phys. Rev. Lett. 116 (2016) 055901.
[25] G. Kresse, J. Furthmüller, Comput. Mater. Sci. 6 (1996) 15.
[26] P.E. Blöchl, Phys. Rev. B 50 (1994) 17953.
[27] G. Kresse, J. Furthmüller, Phys. Rev. B 54 (1996) 11169.
[28] J.P. Perdew, J.A. Chevary, S.H. Vosko, K.A. Jackson, M.R. Pederson, D.J. Singh, C. Fiolhais, Phys. Rev. B 46 (1992) 6671.
[29] G. Henkelman, B.P. Uberuaga, H. Jónsson, J. Chem. Phys. 113 (2000) 9901.
[30] S.P. Ong, W.D. Richards, A. Jain, G. Hautier, M. Kocher, S. Cholia, D. Gunter, V.L. Chevrier, K.A. Persson, G. Ceder, Comput. Mater. Sci. 68 (2013) 314.
[31] Z. Deng, Z. Zhu, I.-H. Chu, S.P. Ong, Chem. Mater. 29 (2017) 281.
[32] H. Cho, H. Son, D. Kim, M. Lee, S. Boateng, H. Han, K.M. Kim, S. Kim, H. Choi, T. Song, K.H. Lee, J. Phys. Chem. C 121 (2017) 14994.
[33] J.E. Saal, S. Kirklin, M. Aykol, B. Meredig, C. Wolverton, JOM (J. Occup. Med.) 65 (2013) 1501.
[34] A. Jain, S.P. Ong, G. Hautier, W. Chen, W.D. Richards, S. Dacek, S. Cholia, D. Gunter, D. Skinner, G. Ceder, K.A. Persson, Apl. Mater. 1 (2013) 011002.